

Ocean bottom friction coefficient from SEASAT–ALT data (Hudson Bay)★

Wooil Moon and Roger Tang *Department of Earth Sciences, University of Manitoba, Winnipeg, R3T 2N2 Canada*

Accepted 1986 July 25. Received 1986 July 14; in original form 1984 April 10

Summary. Ocean bottom frictional coupling has been a complex yet very important problem in global geodynamics. However, due to the logistic difficulties involved, the ocean bottom friction coefficient database has been very sparse and the available data, often from a limited number of installations, represent only a very small number of regions. In this study, a hydrodynamic modelling technique (numerical approach) is extended to accept atmospheric data interactively and the resulting transient sea-surface height information is correlated with the SEASAT–ALT data sets over the Hudson Bay area of Canada. A least squares fitting of the corrected SEASAT–ALT data to the theoretically computed sea-surface profiles then allows us to estimate the ocean bottom coupling coefficients. The representative values for the linear and quadratic ocean bottom friction coefficients are 0.255 and 0.00234 cm s^{-1} respectively.

Key words: ocean bottom friction coefficient, satellite altimetry, SEASAT

1 Introduction

Tidal dissipation at the ocean floor has long been regarded as an adequate explanation for the secular behaviour of the lunar orbit and the Earth's rotation; however, the actual mechanism involved is still a fascinating subject of research. The most common way to evaluate the shallow water dissipation is to find the rate of work per unit surface done by the current on the sea floor (Munk & MacDonald 1960; Lambeck 1975; Brosche & Sündermann 1978). The success of this approach relies on knowledge of the frictional coefficient which links the frictional force at the ocean floor, either quadratically or linearly, with the current velocity (Grant & Madsen 1979; Soulsby & Dyer 1981). Not only is the frictional coefficient important in this context, but a variety of storm surge and tidal modelling problems also require a similar dissipation mechanism (e.g. Grace 1930; Heaps 1969; Pekeris & Accad 1969; Stock 1976; Moon & Tang 1984a, b).

★ The University of Manitoba, Center for Precambrian Studies Publication No. 101.

Most work done on the determination of the bottom stress coefficient, assuming either a quadratic or linear friction law, relies on measurements from a very restricted number of areas. Some of the difficulties involved are primarily due to the logistic problem which limits observations to very few sites on the continental shelf or shallow sea (Bowden & Fairbairn 1956; Sternberg 1968). The primary objective of this paper is to estimate the ocean bottom friction coefficient using a previously developed algorithm for the study of transient sea state in SEASAT altimetry (Moon 1984; Moon & Tang 1984b; Moon, Tang & Choi 1987). Descriptions of the corrections and the available correction algorithms to SEASAT data have been presented by Lorell, Parke & Scott (1980) and Tapley, Born & Parke (1982). With the corrected surface height observations from SEASAT, we can derive a numerical value of the ocean bottom friction coefficient by optimizing the observations with respect to the computed values of the transient sea surface along the satellite orbit tracks. The optimization procedure and preliminary results over selected satellite paths will be presented and discussed.

The magnitude of transient sea-surface variation in altimeter measurements is directly related to the amount of momentum transferred across the air–sea interface from atmospheric disturbances. Since wind stress is shown to be quadratically dependent on wind speed (Kinsman 1965), the hydrodynamic modelling scheme proposed for the transient sea surface height correction will be re-examined together with various recently published quadratic wind stress coefficient formulae. Some recent studies of air–sea coupling will be reviewed and the database of previous studies (Moon & Tang 1984b, 1985) is extended to an additional time period of 1978 August 18–21 during the SEASAT mission. The results of this test provide some insight into the effects of wind stress in transient sea state and on the geophysically acceptable choice of the wind stress coefficient formula used in determining the amount of stress at the air–sea interface. The latter is extremely important in the estimation of the ocean bottom friction coefficient. The topics of the ocean bottom friction coefficient, and coupling processes involving bottom roughness and the sediment transport mechanism have recently become important research subjects (Grant & Madsen 1979; Soulsby & Dyer 1981). The detailed physical processes associated with the geophysical boundary layers will be discussed by Moon (1987).

The second objective of this paper is to update the report (Moon 1984; Moon & Tang 1984b) comparing the SEASAT–ALT inferred wind speed and the geostrophically derived sea-surface wind speed. The number of such comparisons must be sufficiently large to permit statistical evaluation of any discrepancy observed during the correlation. This type of comparison is possible in our study partly because of the size of the wind prediction model and partly because of the available frequency of the SEASAT passes during the selected time intervals included. Since the surface wind fields are derived from the mean sea level (MSL) pressure charts, they are assumed to be good estimates of the ground truth. The results of nearly 690 wind speed comparisons, made during August 4–6 and August 18–21 are presented. We will also present recent results by various authors (Fedor & Brown 1982; Wentz, Cardone & Fedor 1982) to make an objective assessment of our comparison.

2 Review of transient hydrodynamic modelling method

When high precision is desired in a geophysical or oceanographic study involving the utilization of the SEASAT–ALT measurements, elimination of the transient effects due to the sea-surface wind and atmospheric pressure gradients becomes important (Moon & Tang 1984b). Other types of corrections required are described in detail by Tapley *et al.* (1982). The total correction h'_0 can be expressed as:

$$h'_0 = h_0 + \zeta_t + \text{measurement noise}, \quad (1)$$

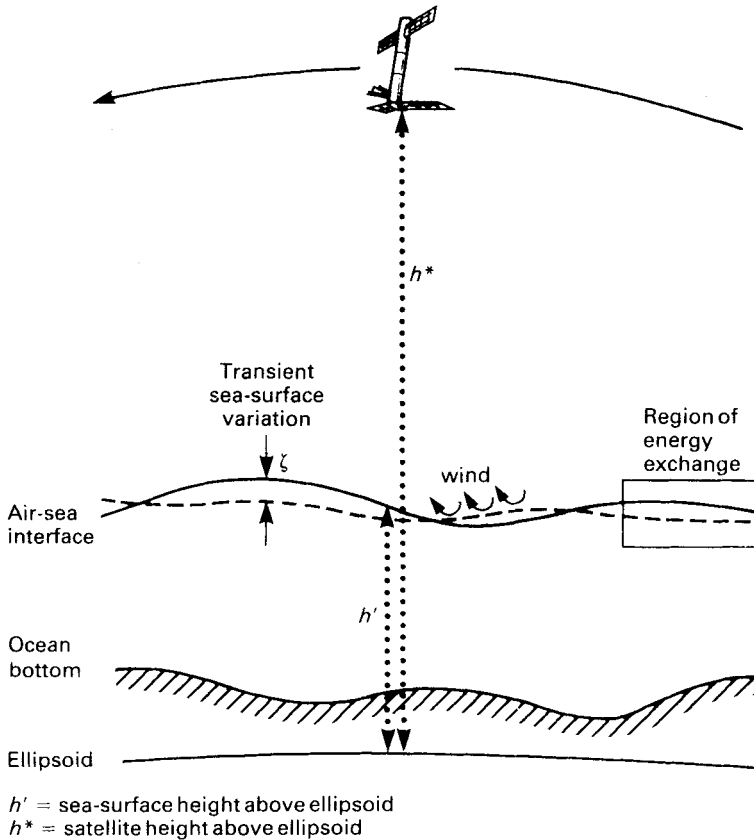


Figure 1. Geometry of the SEASAT-ALT measurement: h' is the sea-surface height above the reference ellipsoid; corrections are applied except for the transient effects.

where the correction h_0 includes the fundamental effects of satellite characteristics, instruments, the atmosphere and the ancillary effects that contain the corrections for the satellite orbit, marine geoid, and solid Earth and ocean tides. The quantity ζ_t in the SEASAT-ALT measurements represents the transient contributions due to barometric pressure variation, ocean surface wind and horizontal pressure gradient. Assessments of the accuracy of these corrections, except for the transient corrections ζ_t , are also summarized in Tapley *et al.* (1982). Fig. 1 shows a simplified sketch of the SEASAT-ALT measurement configuration over the atmosphere-ocean-solid Earth boundary layer system. For the study of mesoscale phenomena, which are characterized by temporal scales ranging from weeks to months, the altimeter (SEASAT-GDR) data sets are acceptable in most cases, even without precise transient corrections. It is well known, however, that the transient sea-surface height variation due to the atmospheric driving force can easily exceed the accuracy specification of the altimeter. This can impose problems for the SEASAT-ALT data users, particularly in the study of regional time-varying sea surface features.

Transient sea surface phenomena can be modelled by solving the hydrodynamic integro-differential equations (Simmons 1980; Moon *et al.* 1987). Consider a water-covered area, large enough so that the curvature of the Earth and the latitudinally varying Coriolis acceleration have to be taken into account. The linearized depth-integrated continuity equation and

equation of motion describing the transient sea-surface height variation are given by:

$$\frac{1}{a \cos \phi} \left\{ \frac{\partial}{\partial \phi} (u \cos \phi) + \frac{\partial v}{\partial \chi} \right\} + \frac{\partial \zeta}{\partial t} = 0 \quad (2)$$

$$\frac{\partial u}{\partial t} + 2\Omega v \sin \phi = -\frac{gH}{a} \frac{\partial \zeta}{\partial \phi} - \frac{H}{\rho a} \frac{\partial P_a}{\partial \phi} + \frac{1}{\rho} (F_S - F_B) \quad (3)$$

$$\frac{\partial v}{\partial t} - 2\Omega u \sin \phi = -\frac{gH}{a \cos \phi} \frac{\partial \zeta}{\partial \chi} - \frac{H}{\rho a \cos \phi} \frac{\partial P_a}{\partial \chi} + \frac{1}{\rho} (G_S - G_B) \quad (4)$$

(Heaps 1969; Zahel 1978) where

ϕ, χ = latitude and east longitude

t = time

ζ = elevation of the sea surface above the equilibrium surface

P_a = atmospheric pressure

u, v = components of the total transport (u parallel to the ϕ coordinate axis and v to the χ -axis)

F_S, G_S = components of wind friction on the sea surface (F_S the component parallel to the ϕ axis and G_S to the χ axis)

F_B, G_B = components of the friction on the ocean bottom

a = radius of the Earth.

H = water depth (Fig. 2)

ρ = density of sea water

g = gravitational acceleration

Ω = Earth's rotation rate.

The above representation is valid when the depth of the water is very much larger than the amplitude of the transient surge. The time-varying sea-surface elevation, ζ , is solved interactively with the atmospheric driving forces, which are derived from the atmospheric pressure gradient and the sea-surface wind. This information is initialized at least 24 hr prior to the expected observation and input at regular intervals. The initialized hydrodynamic equation (equations 2–4) may be solved subject to the following initial and boundary conditions:

$$\zeta(\phi, \chi, t) = u(\phi, \chi, t) = v(\phi, \chi, t) = 0 \quad \text{at} \quad t = 0 \quad (5)$$

and along the shoreline

$$u \cos \psi - v \sin \psi = 0, \quad (6)$$

where ψ is the inclination of the normal to the shoreline to the northerly direction. Along the open boundary, ζ may be specified as a function of position and time representing a surge propagating across the boundary. Fig. 1 shows (schematically) the contribution of transient surge in the SEASAT–ALT measurements. Besides the momentum transfer which takes place at the air–sea interface for the generation of surge, an appropriate expression for the energy dissipation at the sea floor is also required to complete the problem. For this

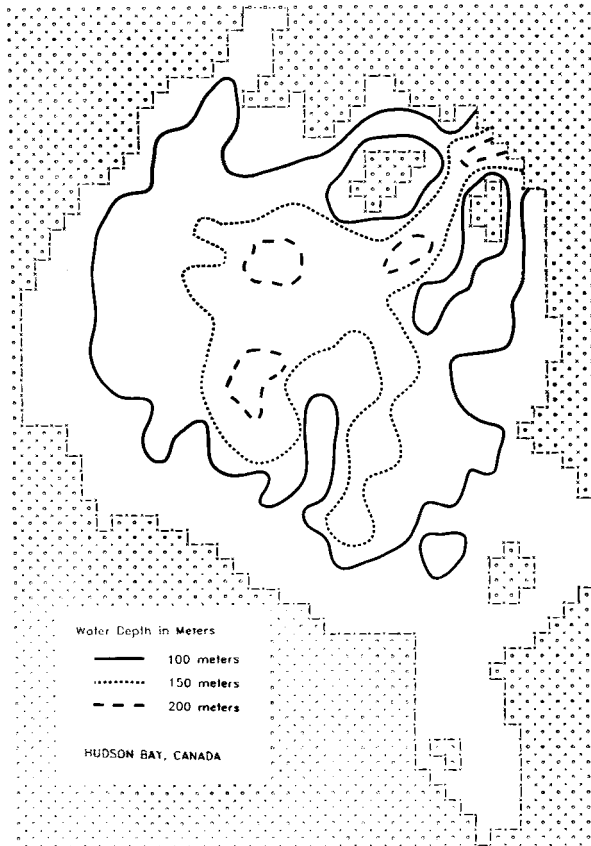


Figure 2. Digitized water depth field of Hudson Bay, Canada.

purpose, the bottom stress law is initially assumed to be linear:

$$F_B = \frac{\eta \rho}{H} u, \quad G_B = \frac{\eta \rho}{H} v, \quad (7)$$

where η is the linear stress coefficient, often assigned a traditional value of 0.24 cm s^{-1} (Weenink 1958). The quadratic friction law later adopted is described in the following sections.

Since equations (2)–(4) cannot be solved analytically, they will be replaced by explicit finite difference representations, and solved numerically with forward and backward difference schemes used in the time domain and a central difference scheme used in coordinate space (Ramming & Kowalik 1980). The staggered finite difference grid of the modelling area (Hudson Bay, Canada) is shown in Fig. 3. Coordinate increments $\Delta\phi$ and $\Delta\chi$ are $0^\circ.12$ and $0^\circ.24$, respectively, and the time increment Δt has been chosen to satisfy the following stability criterion (Heaps 1969; Moon & Tang 1984b):

$$\Delta t < L \left\{ \frac{2}{(gH)^{1/2}} \min(a\Delta\phi, a \cos \phi \Delta\chi) \right\}, \quad (8)$$

where L is the lower bound, and $\min ()$ is the minimum, of a quantity.

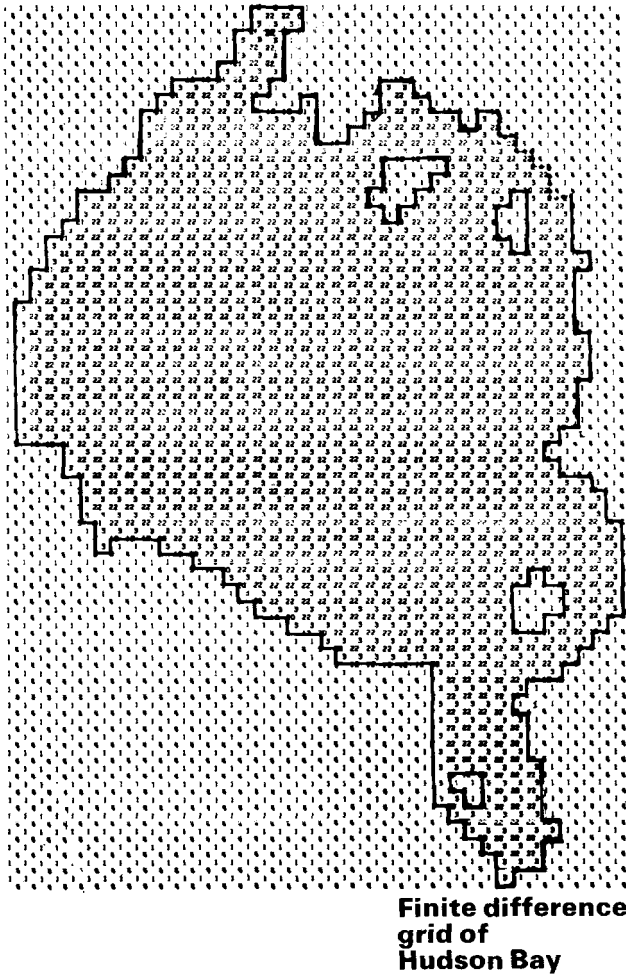


Figure 3. Numerical staggered finite difference grid of the modelling area. The numbers in the grid correspond to different types of boundary.

In general, the iterative solution for the transient sea-surface build-up was very stable and the criteria given above provided only a precautionary guide.

After the necessary input for the iterative modelling has been gathered and determined, the transient sea-surface height is computed at each elevation grid point for successive time steps with interval Δt . Both wind and pressure gradients are input to the iterative procedure at 3 hr intervals (Fig. 4) to simulate the actual weather conditions. The transient sea-surface elevation change can then be computed interactively at any desired instant. For the purpose of simulation accuracy, weather information is input to the algorithm at least 24 hr prior to the first expected output. This allows sufficient time to remove the influence of the initial condition specified in the modelling process.

The transient sea-surface variation has been so modelled over Hudson Bay for the SEASAT-ALT data for revolutions nos. 559, 564 and 574 (Moon & Tang 1984b). The results showed that the transient sea surface deviates from the equilibrium surface by up to approximately 8 cm for wind speeds ranging from 1 to 4 m s⁻¹.

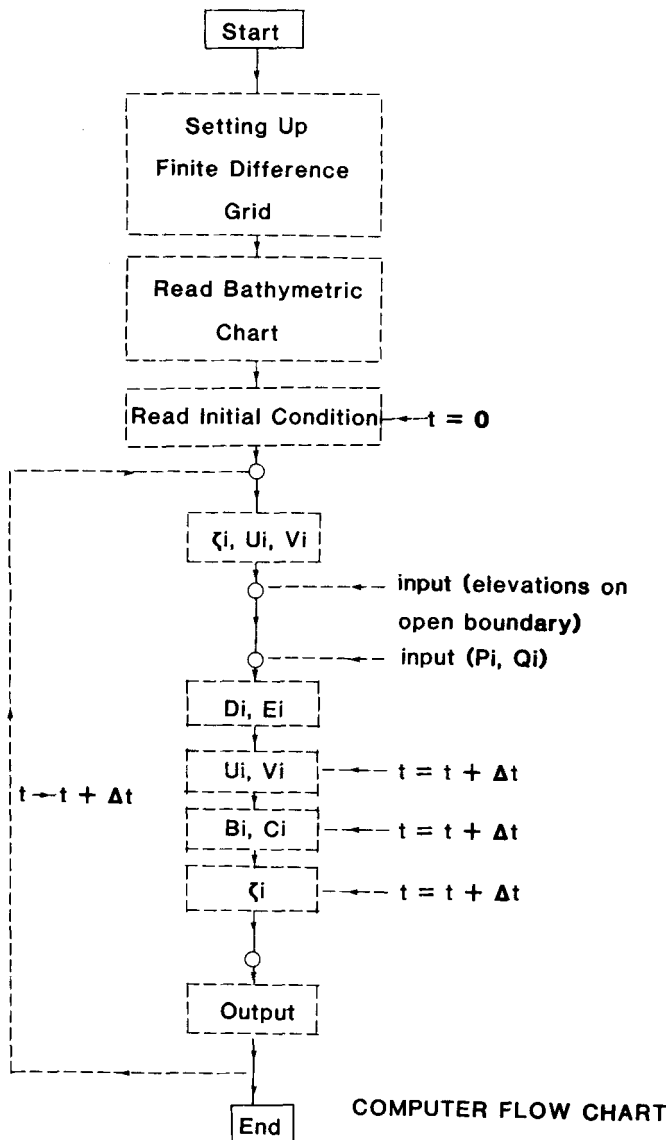


Figure 4. Flow diagram showing the computational procedure for the transient surge. The values of B_i , C_i , D_i and E_i are calculated during the iterative procedure (Moon & Tang 1984).

3 Wind stress at the air–sea interface

Variation in sea-surface elevation and the wind-induced current are directly related by the equations described above and the frictional coupling mechanism at the air–sea interface (Kinsman 1965; Pedlosky 1979; Ezraty 1985). As a result of wind stress, a significant proportion of downward momentum is transferred across the air–sea interface, while the rest is either reflected back to the atmosphere or converted to another form of energy before being transferred into the sea. The coupling mechanism at the air–sea interface remains a challenging theoretical problem, although the magnitude of the coupling strength is believed to be quadratically related to the magnitude of the wind speed. Part of the problem in quantify-

ing the coupling effect lies with the reliability and accuracy of the methods used to estimate wind stress as a function of wind speed. For this reason, the use of the correct surface wind stress remains crucial in modelling the transient surge as well as in the study of global scale oceanographic problems.

Recently, a considerable amount of wind-speed data has been accumulated which has allowed the introduction of several empirical laws in terms of sea-surface parameters (Brocks & Krugermeyer 1972; Wu 1982). Such wind-speed data, and surface parameters derived primarily from shipboard observations, can be used to give a reasonable representation of true surface wind motion. If we assume thermally neutral stability, the surface wind velocity distribution above the sea surface is found to vary logarithmically with height:

$$V(z) = \frac{V_*}{\kappa} \ln \left(\frac{z}{z_0} \right), \quad V_* = \frac{\tau}{\rho_a} \tag{9}$$

where

$V(z)$ = mean wind velocity measured at elevation z above sea surface

κ = von Karman constant (taken as 0.4)

z_0 = vertical intercept of a semilogarithmic plot of z versus $V(z)$ (a measure of surface roughness)

τ = surface wind stress

ρ_a = atmospheric density.

A similar relation is also used to study the ocean bed stress and roughness (Soulsby & Dyer 1981) but with different von Karman constant and with modified boundary layer conditions. The stress τ at the air–sea interface can be determined from the slope of a straight line in the semilogarithmic plot of Z versus $V(z)$ and the averaged value of atmo-

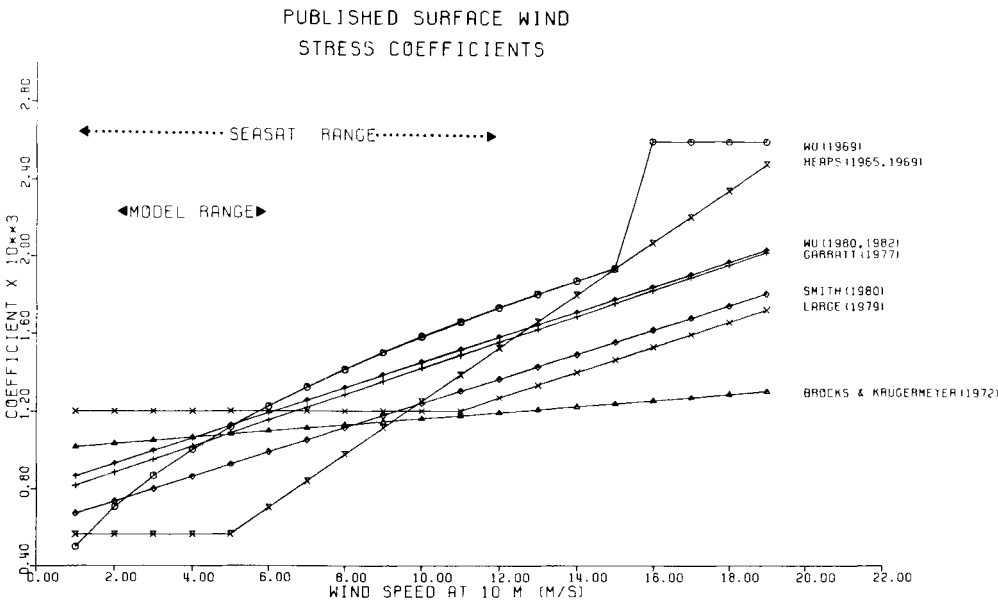


Figure 5. Recently published quadratic wind stress coefficient formulae expressed as a function of wind speed.

spheric density. Because of difficulties involved in the measuring wind velocity at different heights, it has become popular to use the quadratic stress law which combines the wind speed directly with wind stress at a reference height z' , given by

$$\tau = C_z' \rho_a V^2(z). \quad (10)$$

The reference height z' is usually taken to be 10 m above sea level. Equation (10) is an inherently simple, yet important relation between the wind field and the stress it exerts at the air-sea interface. A large number of *in situ*, as well as laboratory, measurements have been made in an attempt to accurately estimate the wind stress coefficient (e.g. Garratt 1977; Smith 1980; Wu 1969, 1980, 1982). Most results show that the wind-stress coefficient depends on wind speed. In his recent study, Ezraty (1985) has demonstrated that the temperature and relative humidity at the sea surface have no significant effect on the wind-stress coefficient, under the conditions of this study. Fig. 5 graphically depicts several relations published recently. Typical ranges of wind speed as found from both SEASAT-ALT GDR file and the atmospheric model used in this study are also indicated. One of the more comprehensive investigations was done by Wu (1969) using some 30 independent oceanic observations. In recent reviews of old data, Wu (1980, 1982) proposed a new wind-stress coefficient formula, given by

$$C_z' = (0.8 + 0.065 |\bar{V}_d|) \times 10^{-3}, \quad (11)$$

where $|\bar{V}_d|$ is the magnitude of the derived sea surface wind at the reference height $z' = 10$ m. He showed that the formula was applicable to both strong ($> 15 \text{ m s}^{-1}$) and light ($< 15 \text{ m s}^{-1}$) wind. The formula is very similar to that obtained by Garratt (1977) from data based largely on Reynolds stress and wind profile measurements. Although most of the formulae depicted in Fig. 5 suggest that the wind-stress coefficient is linearly related to wind stress (e.g. Garratt 1977; Smith 1980; Wu 1980, 1982), it is likely that this is a considerable simplification of reality. A suitable formulation of wind stress at the sea surface is of particular importance because the amount of energy dissipated at the sea floor depends directly on the momentum transferred by surface stress. Thus various formulae representing wind-stress coefficient will be reviewed in this research in order to investigate their influences on the simulation of transient sea-surface dynamics.

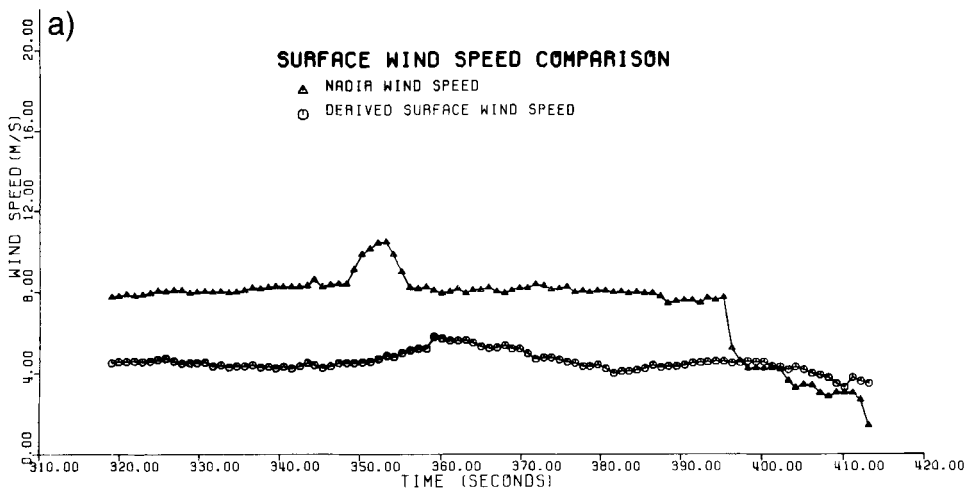


Figure 6. Wind speed profiles along the SEASAT orbit tracks over Hudson Bay during August 18-21. Diagrams (a), (b), (c) and (d) are for satellite revolutions nos 760, 765, 779 and 789.

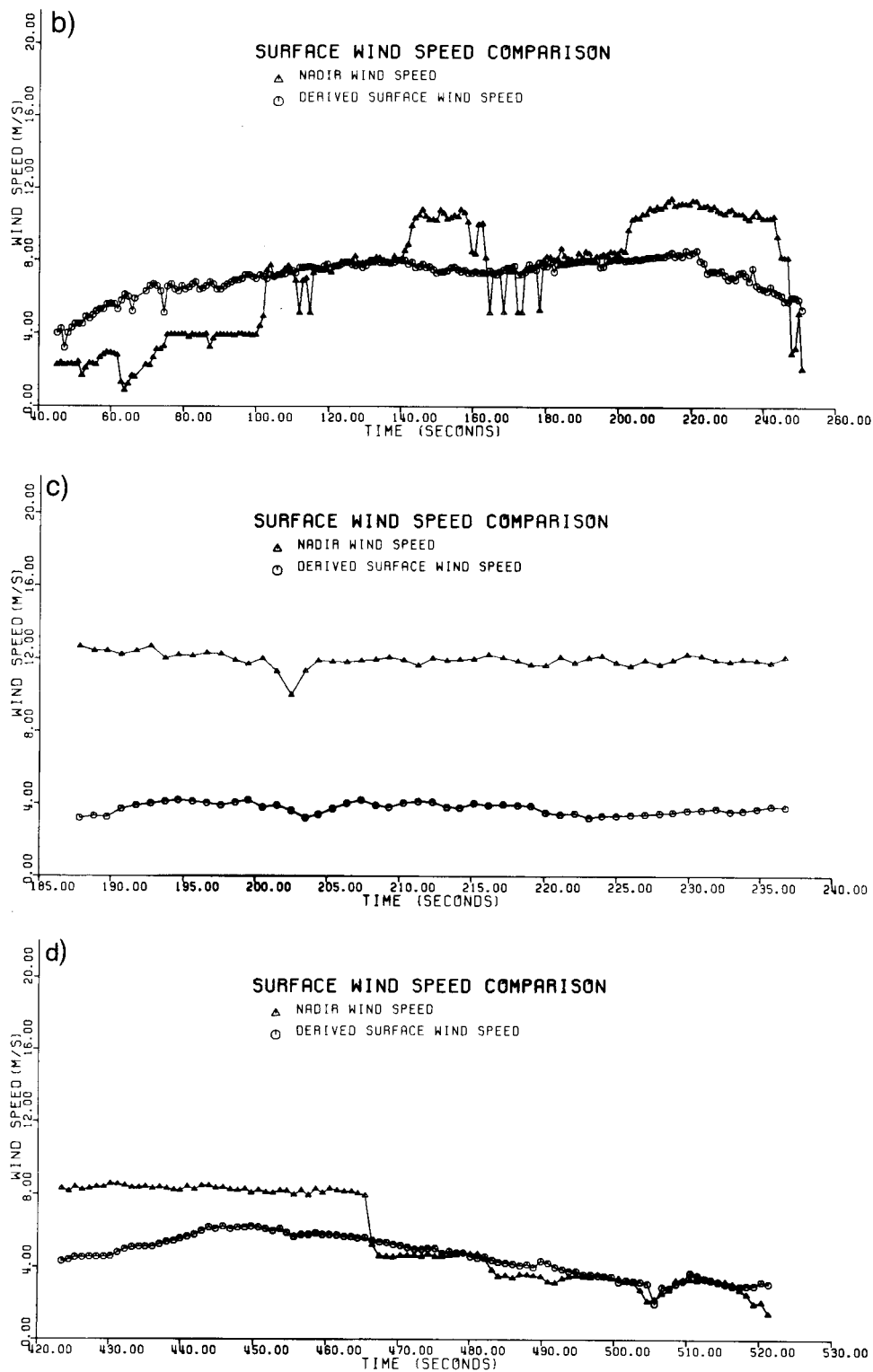


Figure 6 – continued

4 On wind speed from SEASAT GDR and atmospheric pressure charts

In the transient sea-surface simulation, the wind field over the sea surface has to be prescribed as a function of time and spatial coordinates. The usual method of accomplishing this is by dividing the studied area into subareas in which a constant and uniform atmospheric steady state is assumed. Obviously, this is a very time-consuming task and would not be very accurate in the vicinity of sharply curving isobars such as are often encountered in real situations.

The numerical method used to derive the sea-surface wind field from the MSL pressure charts (Moon & Tang 1984b) is based on the assumption of geostrophic flow and an empirical relation, obtained by Hasse & Wagner (1971), which converts the geostrophic wind to surface wind. The method also takes the Coriolis force and sea-surface friction into account and is considered to give a good estimate of the surface truth. On the other hand, the wind speed inferred from the SEASAT ocean surface backscatter coefficient using the three-branch logarithmic algorithm of Brown, Stanley & Roy (1981) has been shown to yield unbiased wind when compared to the estimates made from the SEASAT-SMMR (Scanning Multichannel Microwave Radiometer) data as well as from the buoy measurements (Fedor & Brown 1982). In the following discussion a more detailed comparison will be made between the geostrophically derived sea-surface wind and the satellite altimeter inferred wind.

Table 1. Statistics of wind speed comparisons.

Revolution number	Model range (m s ⁻¹)	SEASAT range (m s ⁻¹)	Number of comparisons	Mean difference (m s ⁻¹)	Standard deviation (m s ⁻¹)
559	2.0–4.5	2.0–9.0	92	2.27	2.00
564	4.0–5.0	1.0–9.5	189	2.55	2.15
574	1.0–4.0	1.0–3.5	92	–0.20	0.90
760	4.0–5.0	3.0–9.0	97	2.79	1.73
765	3.0–8.0	1.0–10.0	209	0.09	2.38
779	2.5–4.0	10.0–13.0	51	8.18	0.48
789	2.0–6.0	2.0–8.0	101	1.00	1.63

Figs 6a–d depict the SEASAT-ALT inferred wind speed profiles along the selected SEASAT orbit tracks which are superimposed on the interpolated wind profiles obtained from the MSL pressure charts supplied by Environment Canada. Table 1 gives the comparison statistics, i.e. the ranges of wind speed, the number of samples, the mean difference, and the standard deviation. The correlation of the two wind fields is reasonably good for revolutions nos. 574, 765 and 775. Fig. 7 is a residual frequency plot of the difference of the two data sets for wind speed below 10 m s⁻¹. The general shape of the histogram follows a normal distribution with the maximum located at zero residual.

Table 2 summarizes the overall statistics for all the revolutions along with the results obtained by other authors (Wentz *et al.*, 1982; Fedor & Brown 1982) for comparison. The first three rows of Table 2 were obtained by Wentz *et al.* (1982) using the wind speeds retrieved from the SEASAT scatterometer (SASS), altimeter (ALT) and radiometer (SMMR). Although they concluded that the SASS, ALT and SMMR winds agree with the *in situ* anemometer measurements, the size of the data sets is very limited and this introduces some statistical uncertainties into the results. For the 87 comparisons made between the buoy measurements and satellite altimeter inferred wind speeds (Fedor & Brown 1982), a mean

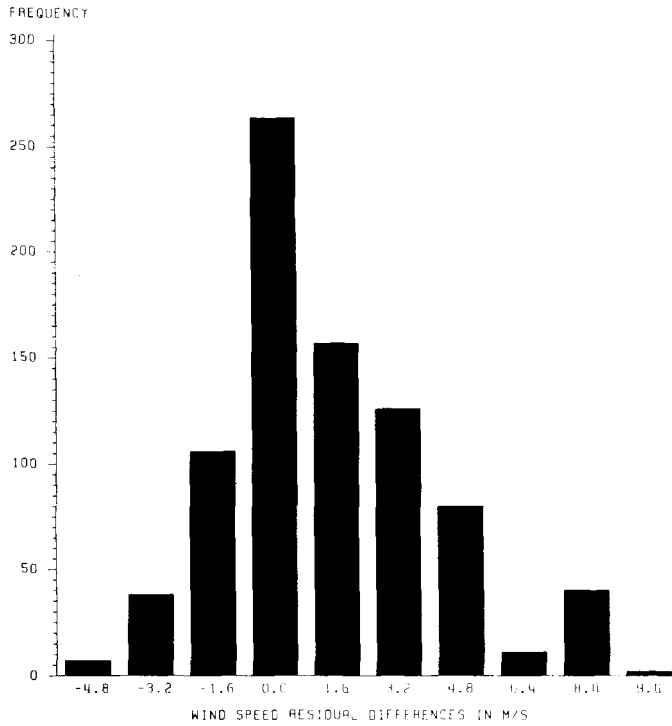


Figure 7. Histogram of residual values of the SEASAT–ALT inferred wind speed and the geostrophically derived sea-surface wind speed.

Table 2. Summary of different type of altimeter inferred wind speed comparisons.

Comparison type	Number of comparisons	Mean difference (m s ^{−1})	Standard deviation (m s ^{−1})	Authors
ALT–Anemometer	6	−1.64	1.62	Wentz <i>et al.</i> (1982)
ALT–SMMR	6	3.08	1.67	Wentz <i>et al.</i> (1982)
ALT–SASS	5	−3.33	2.31	Wentz <i>et al.</i> (1982)
ALT–Buoy	87	−0.25	1.60	Fedor & Brown (1982)
ALT–MSL	689	1.41	1.80	This paper

difference of -0.25 m s^{-1} and a standard deviation of 1.6 m s^{-1} were estimated over the range of $1\text{--}10\text{ m s}^{-1}$ (Table 2). One way to minimize this discrepancy is to increase the size of the data set. Because of the nature of the wind speed prediction model, it has been possible to compare considerably more data points along the satellite orbit tracks for a period of several days. The results shown in the last row of Table 2 are obtained from the revolutions listed in Table 1 (except for revolution no. 779) with wind speeds ranging from 1 to 10 m s^{-1} .

Further statistics for the altimeter retrieved and the geostrophically derived sea surface wind speeds along the SEASAT orbit tracks are tabulated in Table 3. The percentage reduction from the mean altimeter inferred wind magnitude \bar{V}_s to the magnitude of the MSL derived wind \bar{V}_d is

$$\Delta_{\text{mean}} = \frac{|\bar{V}_s| - |\bar{V}_d|}{|\bar{V}_s|}.$$

(12)

Table 3. Present reduction Δ_{mean} required to reduce the mean altimeter-inferred wind to model-derived wind.

Revolution number	$ \bar{V}_s $ (m s^{-1})	$ \bar{V}_d $ (m s^{-1})	Percentage of reduction	Period reduction (per cent)	Total reduction (per cent)
559	6.19	3.91	36.8		
564	7.10	4.53	36.1	22.2	
574	2.73	2.91	-6.5		27.5
760	7.36	4.45	37.9		
765	7.25	7.15	1.4	31.53	
779	12.05	3.89	67.9		
789	5.75	4.65	18.9		

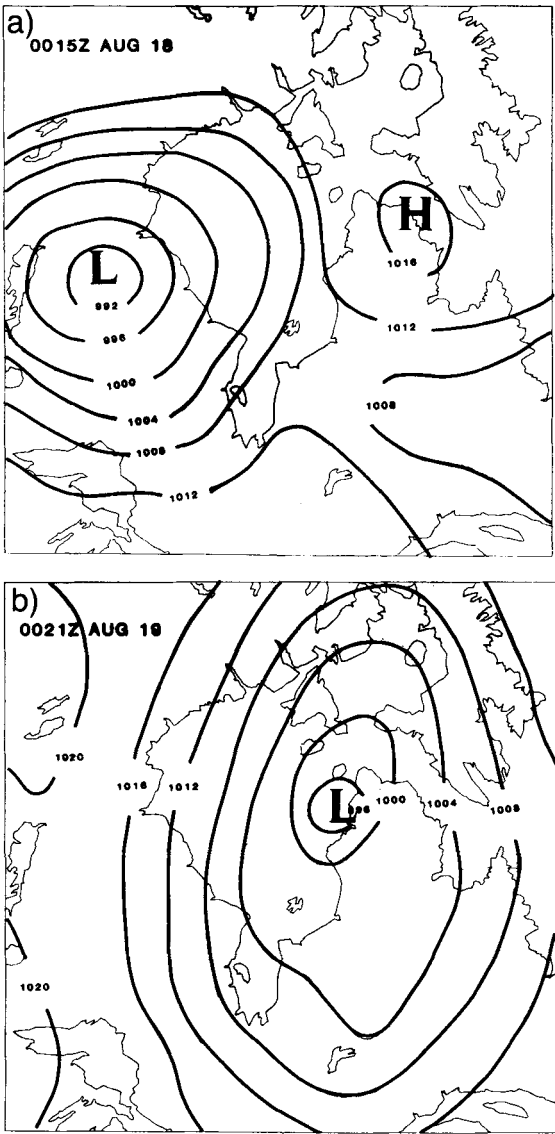


Figure 8. Weather charts for the transient surge modelling for the period 1978 August 18–21.

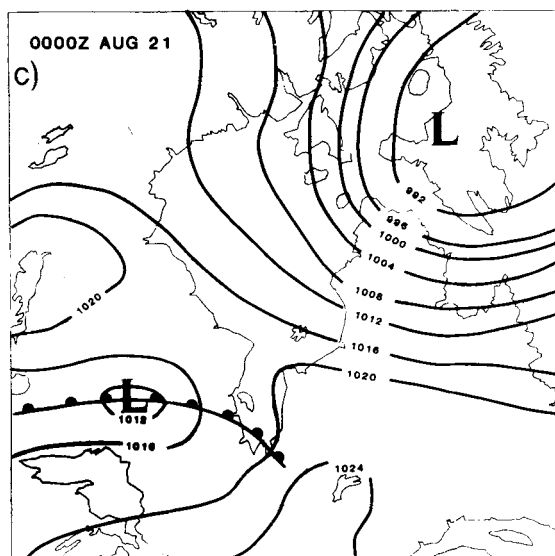


Figure 8 – continued

In almost all cases, $|\bar{V}_d|$ is less than $|\bar{V}_s|$ as shown in Table 3. The averaged reduction for all the selected SEASAT orbit tracks is approximately 28 per cent.

5 Numerical simulation of sea-surface profiles

The MSL pressure charts used in this research are produced regularly at 3-hr intervals and are based on observations from ground stations and weather satellites. Figs 8a–c show three sample weather charts during the SEASAT mission period August 18–21. The charts show a

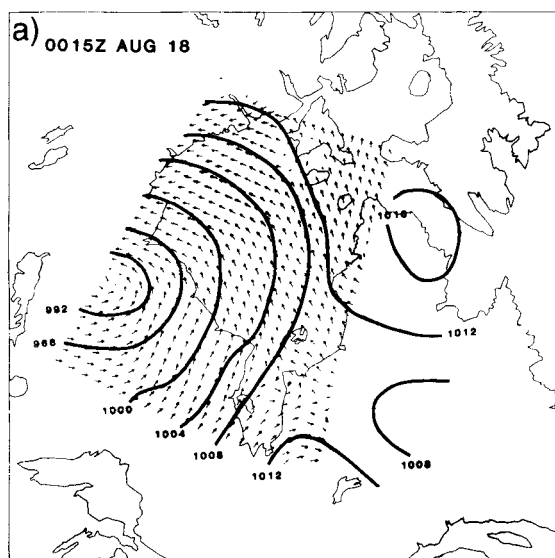


Figure 9. Sea-surface wind fields derived from the weather charts of Fig. 8. The wind speed ranges from 1 to 8 m s^{-1} .

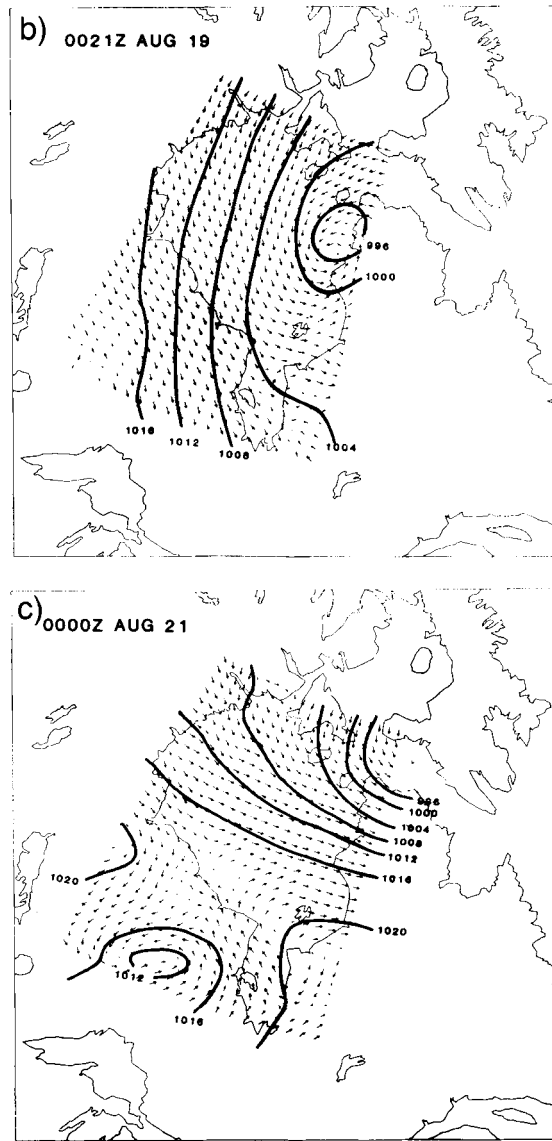


Figure 9 - continued

depression with a centre of varying pressure magnitude moving across Hudson Bay. Figs 9a–c show the geostrophically derived sea-surface wind field. The magnitude of the sea-surface wind is taken as being approximately 60 per cent of the geostrophic wind and the angle between the geostrophic and surface wind vectors is assumed to be 20° . The wind speed associated with these plots ranges from 1 (dots) to 8 m s^{-1} . For illustration, the wind vectors are plotted at every second stream point of the sea model grid and are interpolated from the sea-surface wind field using a cubic Lagrangian polynomial.

The SEASAT orbit tracks for August 4–6 (solid lines) and August 18–21 (dashed lines) are shown in Fig. 10. Some of the tracks are deleted in this study due to their coverage over shallow coastal water where the hydrodynamic solution may suffer from the effects of non-

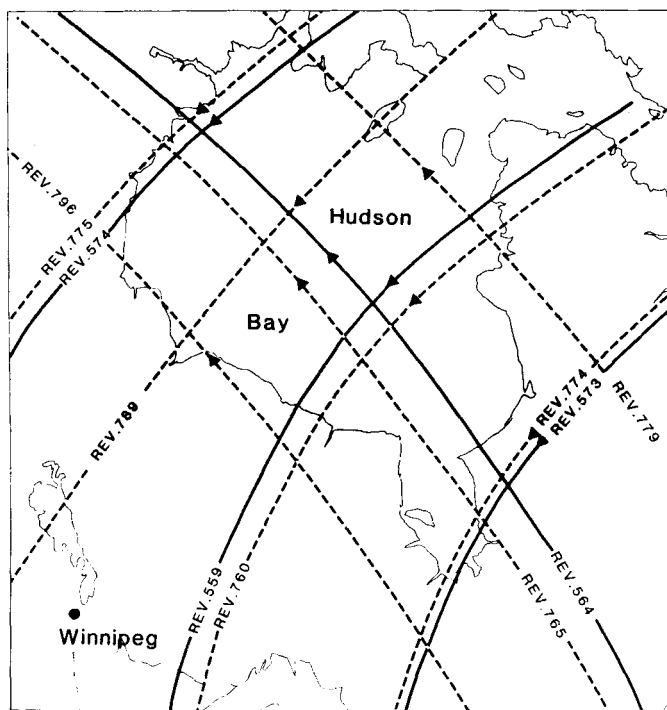


Figure 10. SEASAT orbit tracks over Hudson Bay, Canada, during August 4–6 and August 18–21. The data from both periods are used in wind speed comparisons.

linearity. They include path 8 (revolution no. 578) from August 4–6, and path 11 (revolution no. 774), path 12 (revolution no. 775) and path 24 (revolution no. 796) from August 18–21.

During each time step of the iterative procedure, the wind speed is quadratically converted to wind stress as an external forcing function. A number of wind stress coefficient formulae were tested in the simulation before finally adopting Wu's formula (Wu 1980, 1982). Although the stress produced by the Brocks & Krugermeyer (1972) approach is about 2.5 times larger than that calculated by Heaps (1965, 1969, 1982), at 3 m s^{-1} wind speed (a typical speed value for the period of August 4–6) an averaged change in sea-surface height of less than 1.5 cm is observed in simulations. Similar results were obtained from higher wind speed environments (August 18–21) in which the wind stress computed using Wu's formula (Wu 1980, 1982) is about twice as large as the one predicted by Heaps (1965, 1969) at wind speed of 6 m s^{-1} . These results of relatively small change in sea-surface height imply that different choice of wind stress coefficients at the air–sea interface is not too critical for the ranges of wind speeds and spatial extent of the model area tested in this research.

The transient sea surfaces along the satellite orbit tracks are computed using both quadratic and linear bottom stress laws. For the test run, values of 0.0025 and 0.24 cm s^{-1} , respectively, are used. Two features are observed in the test simulation. (1) The peak to trough amplitude of the sea-surface wave oscillation associated with quadratic bottom friction is considerably larger than that generated using the linear bottom stress law. The magnitude of oscillation increases with decreasing water depth as the theory predicts but the wavelength remains approximately the same in both cases. (2) The absolute difference

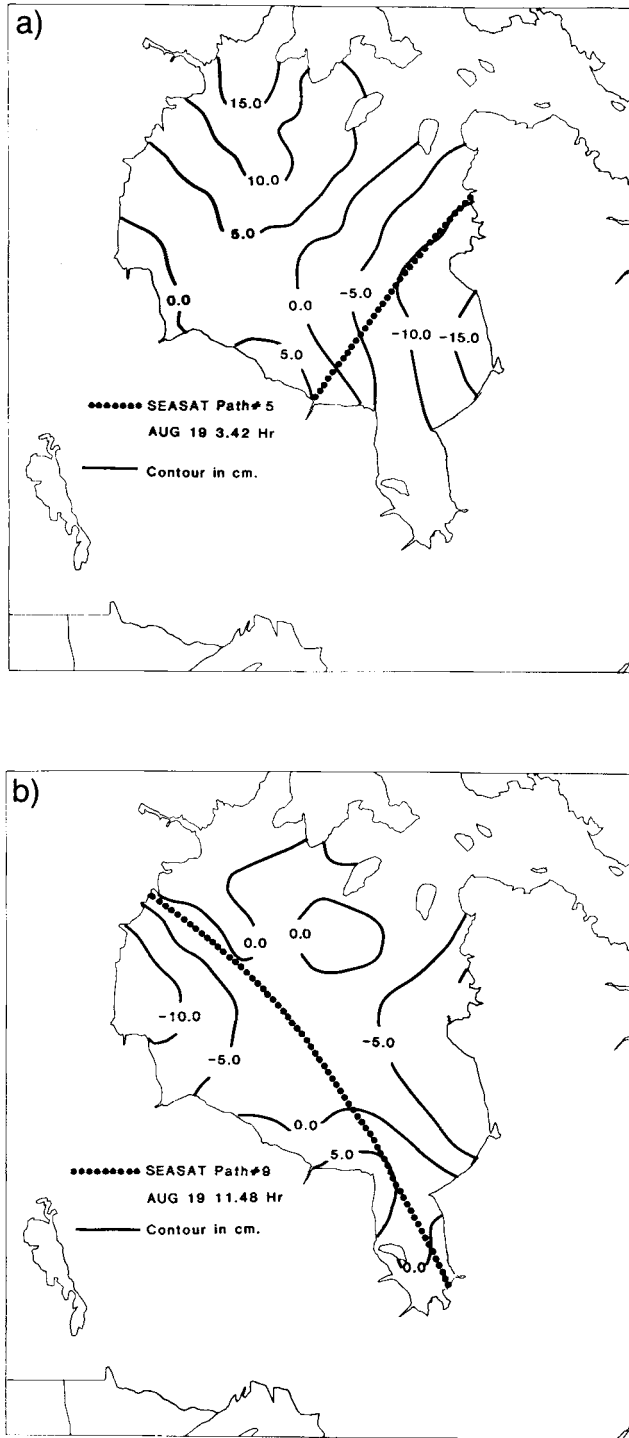


Figure 11. Contour diagrams of the transient sea surface during the time when the satellite is directly above Hudson Bay. Diagrams (a), (b), (c) and (d) correspond to revolutions nos 760, 765, 779 and 789. These contours are produced using the quadratic wind stress coefficient formula proposed by Wu (1980, 1982) and a linear bottom stress coefficient of 0.24 cm s^{-1} (Weenink 1958).

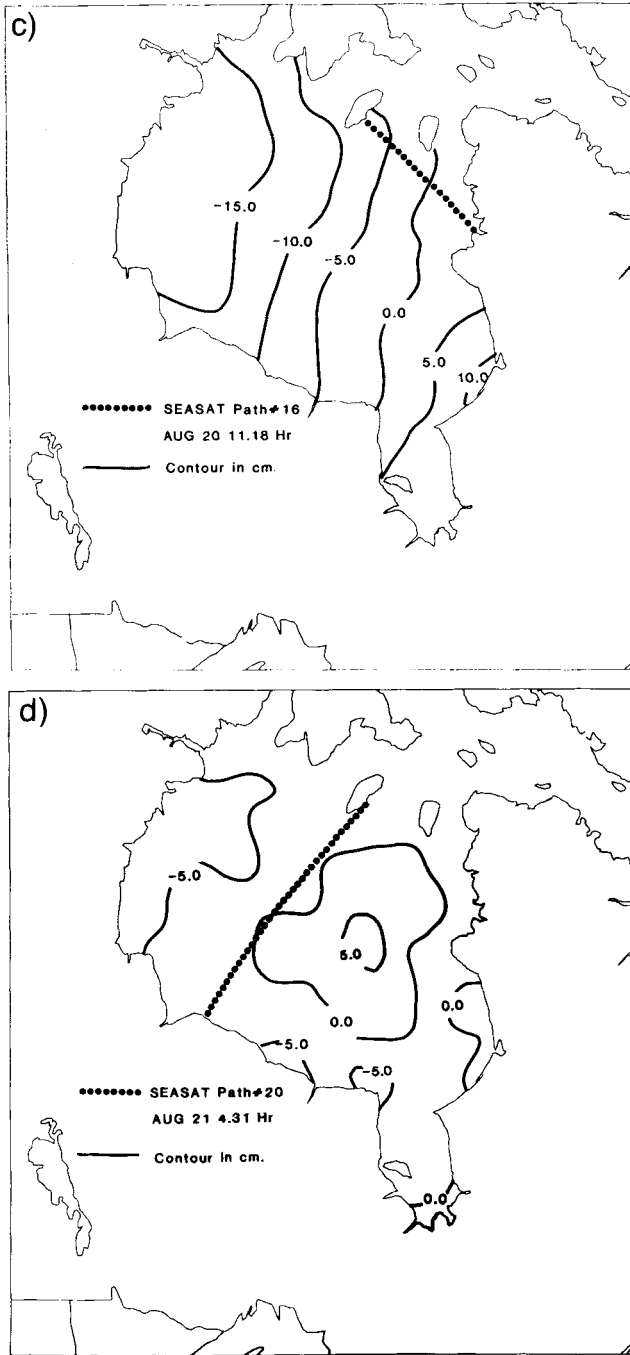


Figure 11 – continued

between the sea-surface heights resulting from assuming either law also varies with depth. The shallower the water, the larger the difference in computed sea-surface elevations. In spite of these differences in numerical characteristics, the general dynamical features and the spatial distribution patterns remain much the same.

Figs 11a–d show the spatial distribution of the transient sea-surface elevation while the satellite was in the middle of its tracks over Hudson Bay. The dotted lines in these diagrams are the footprints of the satellite. An attempt was made to follow the development of the spatial distribution due to the atmospheric disturbance. However, examination of successive distributions did not reveal any clear trend in the changing distribution. This indicates that the atmospheric disturbance is not coupled in any simple way to the sea-surface topography. The contours in the diagram show the averaged change in transient sea-surface topography reaches up to 15 cm during the periods studied. Figs 12a–d are the simulated transient sea-surface profiles along the selected paths for the period August 18–21. Path number 5 (revolution no. 760) exhibits the maximum sea-surface elevation change of up to 14 cm, whereas path number 20 (revolution no. 779) shows a variation of up to 5 cm only.

6 Geoidal undulation in the Hudson Bay area

Before applying the least squares optimization approach which combines the corrected SEASAT–ALT data with the modelled sea-surface topography, we have to investigate

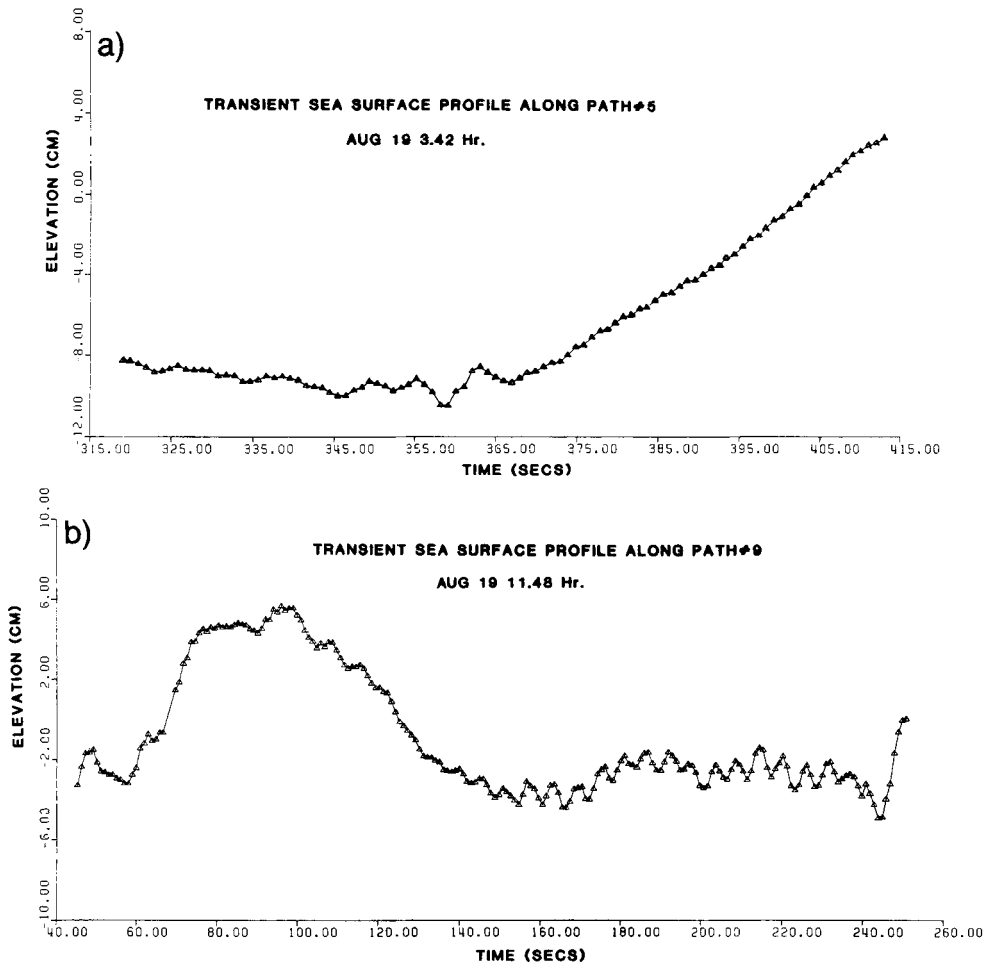


Figure 12. The transient sea surface profiles along the selected revolutions over Hudson Bay during the period August 18–21. The variations correspond to the values along the footprints shown in the Fig. 11.

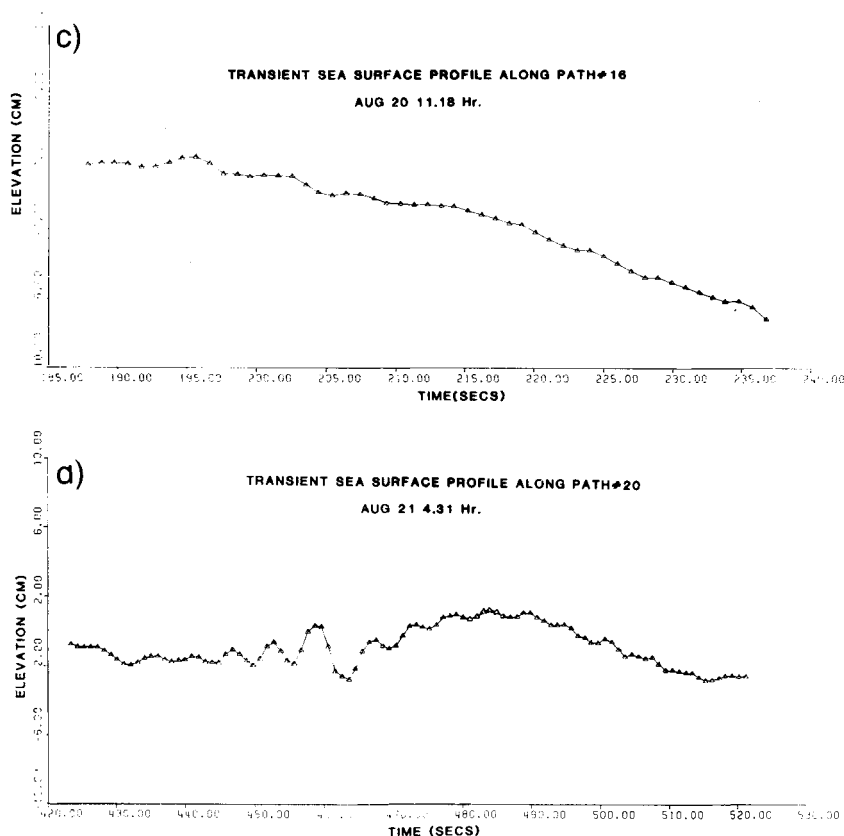


Figure 12 — continued

geoidal anomalies over the area. The sea-surface height given by the SEASAT–GDR tape is an averaged value of measurements for 1 s duration, which represents sampling of the surface along a distance of approximately 7 km. Therefore, according to the Nyquist criterion, the smallest resolvable wavelength in the measurements along the tracks is about 14 km (a distance of three consecutive points). Small-scale geoid anomalies of this order could be very important because they can contribute to observations that cannot be accounted for in the sea model. Since the mean sea surface (SS3) is used for the reduction of observations and since all the shallow water regions of non-linear errors are discarded in the computations, only the geoidal signatures near the centre of the orbit track need to be considered. Fig. 13 shows five geoid profiles, two tracks from August 4–6 and three tracks from August 18–21. These profiles are derived from the GEM 10B geoid which was included as part of the geophysical algorithm (G-7) in the SEASAT–ALT–GDR file (Lorell *et al.* 1980). The profiles depicted in this figure clearly indicate the lack of short wavelength anomalies, as expected from the fact that the only known tectonic feature in this area is the post-glacial isostatic uplift with length scale comparable to the entire Hudson Bay and surrounding area (Andrews 1974; Cathles 1975).

Although GEM 10B was completed only to harmonic degree and order 36, it was one of the more suitable models available for geophysical use. For the reduction of geodetic applications of SEASAT data, other models that contain shorter wavelength information may be

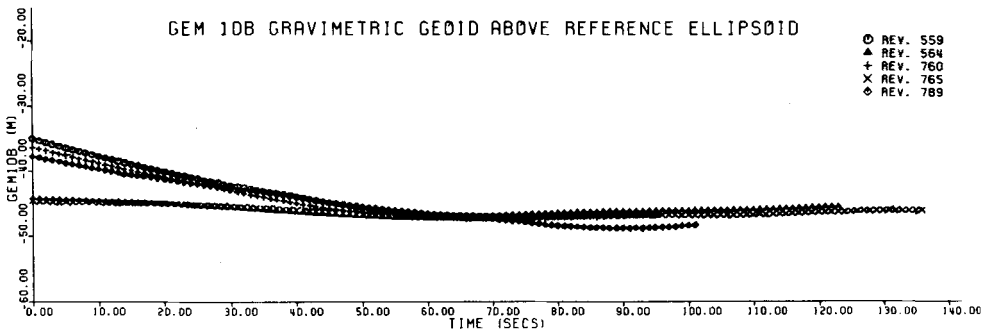


Figure 13. Geoid profile over Hudson Bay along the SEASAT orbit tracks as shown in Fig. 10.

preferred, and a considerably more accurate and detailed model should be derived from future satellite altimeter data. With the data presently available, an attempt was made in this study to estimate the short wavelength anomalies by comparing the GEM 10B with the SS3 altimeter-derived sea surface. However, the wavelength of each of the orbital residuals is still long enough to have no significant effect on the much shorter wavelength dynamic features in the Hudson Bay area.

7 Ocean tides in Hudson Bay

The ocean tide plays a very important role in satellite altimetry, particularly as the accuracy of the new space-borne instruments have been improved. Cartwright & Alcock (1981) reported that the SEASAT data can be used to detect sea-surface slopes of up to 9 cm in 1° of arc and tidal constituents of amplitude up to 10 cm. In this research we have not tried to measure the sea-surface slope, the transtidal waves (Kinsman 1965) or the height of tides with respect to the reference ellipsoid, but have aimed to fit the sea-surface topography as seen by the SEASAT altimeter with the theoretically predicted surface, in the least-squares sense.

The tides in Hudson Bay and the adjacent sea have been studied previously by Freeman & Murty (1976), Schwiderski (1978), Griffith, Pingree & Sinclair (1981) and others, using a numerical method. Tide information available from about 50 stations surrounding the study area can be obtained from the Hydrographic Service of Canada (Ku 1982, 1984). In this research, the results of Freeman & Murty (1976) and Schwiderski (1978) were examined with the observed data. Even though some values of the Schwiderski (1978) ocean tide model for Hudson Bay are known to be not sufficiently accurate, they are illustrated in Fig. 14 to display the overall contribution of tides along the SEASAT tracks studied. In the perspective of time series analysis, these signals (Fig. 14) are of very long wavelength, with the dashed lines (revolutions nos 765 and 564) indicating linear trends. If these characteristics are a reasonable expression of the real tidal contribution, the tidal contribution, corresponding to the revolutions nos 789, 760 and 559, will add a constant linear trend to the altimeter measurements. In the surface fitting of the SEASAT data with the theoretically simulated sea surface, this type of linear shifting can be viewed as a conditioning of data base correlation. In the cases corresponding to revolutions nos 765 and 564, the long wavelength tidal undulation is not only significant in its contribution to the actual sea-surface elevation, but may also indicate considerable hydrodynamic interaction. In this study, the numerical algorithm was not set for the study of hydrodynamic interactions and these will not be dis-

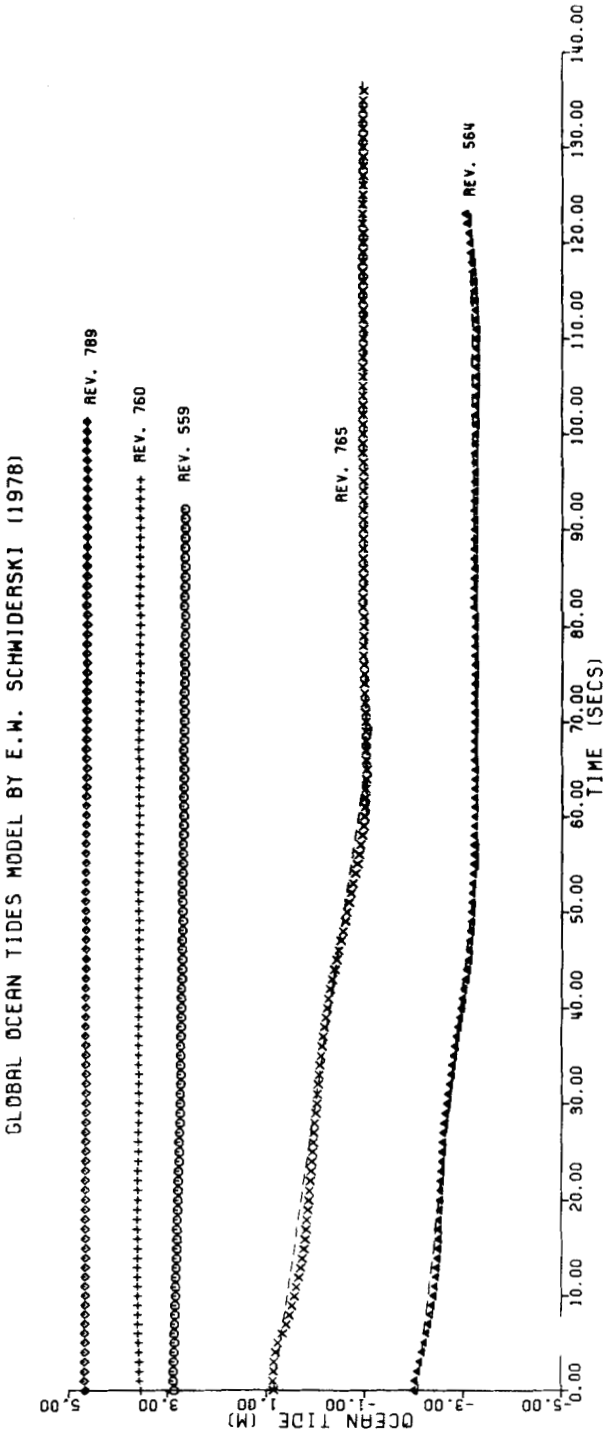


Figure 14. Tidal height interpolated from the Schwiderski Global Ocean Tide model (1978) along the SEASAT orbit tracks as shown in Fig. 10.

cussed (Zahel 1978). However, it was found that, as long as the tidal contribution was removed as a part of correction or was added in computing the theoretical sea-surface elevation above the reference ellipsoid, there was no difference in the estimated final ocean bottom coupling coefficient. This was more or less expected since the numerical process of correlation between the observed SEASAT-ALT data and the computed elevation should depend only on the sea-surface topography but not on the absolute height above the reference ellipsoid. In computing the error due to the short wavelength sea-surface variations along the orbit tracks, the short wavelength tidal contribution was found to be not too significant in the study area, due to its negligible amplitude. It seems determination of the ocean bottom friction is insensitive to geoidal and tidal adjustments in the Hudson Bay area, though they may play a very significant role in other parts of the world (Moon *et al.* 1987).

8 Ocean bottom friction coefficient

In general, two approaches can be employed to determine the ocean bottom friction coefficient. The direct and usual approach is to use measured components of the current velocity to estimate the Reynolds stress across the ocean bottom (e.g. Bowden & Fairbairn 1956). The computed stress may then be equated to a quadratic or linear bottom friction law.

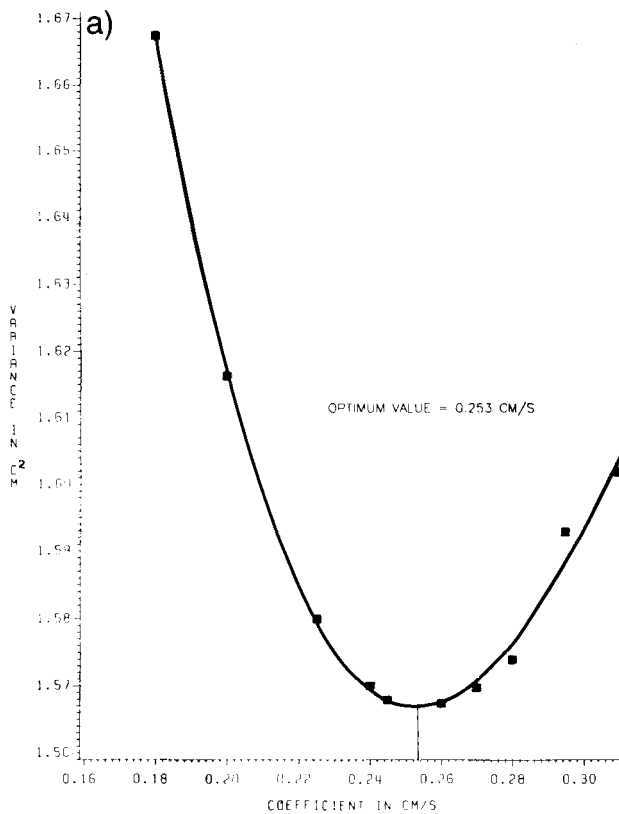


Figure 15. (and overleaf) Variance between simulated and observed transient sea-surface profiles as a function of the constant linear friction coefficient. Diagrams (a), (b), (c) and (d) correspond to revolutions nos 559, 564, 765 and 789.

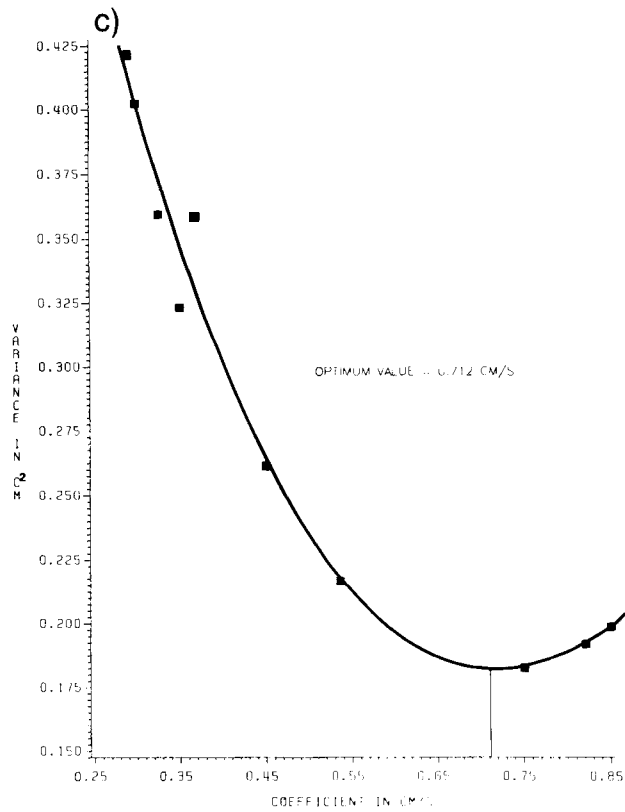
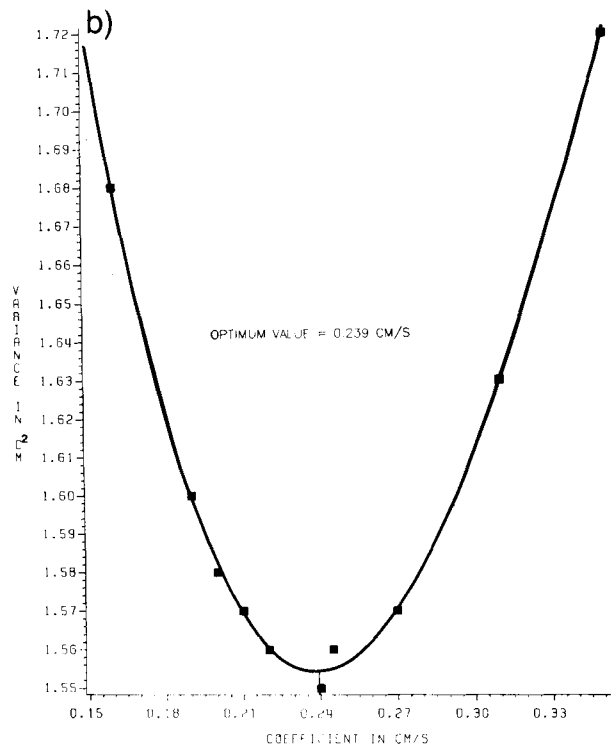


Figure 15 – continued

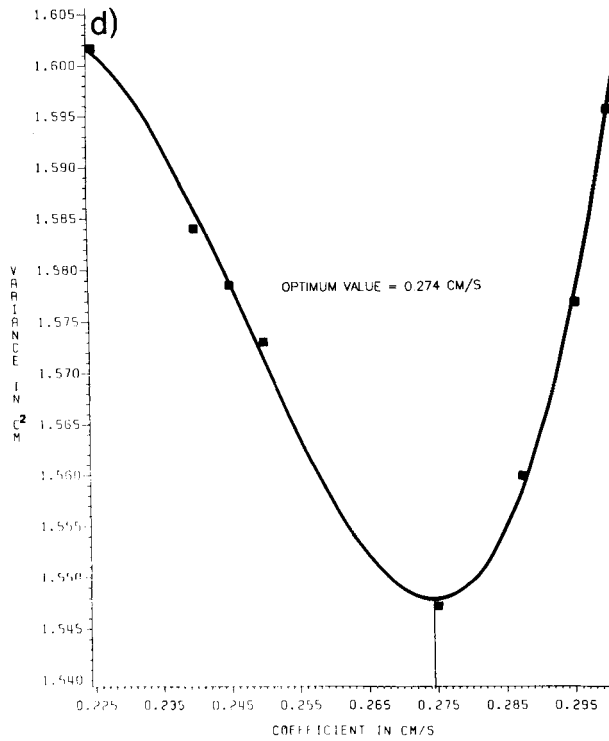


Figure 15 - continued

Among the main disadvantages of this approach are the difficulties associated with the installation and accessibility of equipment in a deep ocean environment. The indirect modelling approach uses theoretical calculations and compares the theoretical results with observed data collected at several available study areas. For example, Grace (1930) obtained a suitable value for the linear stress coefficient by comparing observations with his ocean tidal modelling of the Gulf of Suez. This approach could have been made easier if a massive number of observations were available. The SEASAT mission provided such an opportunity.

We can express the transient sea surface variation ζ_t as

$$\zeta_t = h_{ap} + h_w + h_{pg}, \quad (13)$$

where

h_{ap} = inverse barometric effect

h_w = surface wind effect

h_{pg} = horizontal pressure gradient effect.

The significance of the time-varying solid Earth and ocean tides in the transient sea-surface effect often depends on locality. For example, the contribution of marine tide in Hudson Bay is relatively less important in this study while it could be very important in some other areas (Griffith *et al.* 1981; Moon *et al.* 1987). In such a case, the modelling of tidal amplitude and its interaction with transient surge should be considered. The inverse barometric effect in equation (13) can be estimated using the hydrostatic relation:

$$h_{ap} = -g\rho_a(P_a - 101\,300\,N\,m^{-2}). \quad (14)$$

Thus, by combining equation (14) and the hydrodynamic modelling scheme, the total transient sea-surface variation can be computed for comparison with the SEASAT–ALT measurements. Furthermore, if the SEASAT–ALT measurements can be assumed to be exact, the raw measurements after the application of necessary corrections should provide information on the sea-surface elevation due to the transient effects. It should, however, be understood that equation (13) is an idealized description of the transient sea state. The unmodelled long wavelength errors in the satellite orbit are not important for this research because, being of the order of semi-cyclic per satellite revolution (Marsh & Williamson 1980), they would have the effect only of local ‘DC’ shifting in the SEASAT–ALT data segments used here.

8.1 LINEAR BOTTOM FRICTION COEFFICIENT

The linear bottom stress law is given by equation (7). Probably the only justification for using the linear bottom friction law is its mathematical simplicity. In storm surge and tidal modelling studies, the linear law has provided acceptable results (Grace 1930; Heaps 1969; Pekeris & Accad 1969). The wind stress coefficient formula (equation 10) is used as described in the previous sections to study the transient sea-surface height variation as a function of the linear bottom stress coefficient η . The results from this study involving both SEASAT orbit periods show a general decrease of transient surge amplitude as η increases. The smoothness of the sea-surface topography also seems to be directly proportional to η . Not only is η important in the transient sea-surface elevation simulation, but a proper value of it is also essential to the ocean tidal models invoking the assumption of (7) (Grace 1930; Pekeris & Accad 1969).

A proper value for η is determined by minimizing the difference between the computed and SEASAT measured transient sea-surface elevations for each incremental successive choice of value for η . A similar approach, based on the numerical solutions of the Laplace’s tidal equations and *in situ* observations, was used by Stock (1976) to model different tidal constituents in the Gulf of California. Since the transient sea-surface profiles can be computed at any instant when the satellite is directly over Hudson Bay, a constraint is required to determine the amount of such ‘DC’ shifting. With the assumption that the interpolation between the spatial coordinates is reasonably accurate, the goodness of fit between the model ξ_c^i and the observed ξ_0^i is defined by

$$V_a^i = \frac{1}{2N} \sum_{n=1}^N |\xi_0^i(\eta') - \xi_c^i(\eta_j)|^2, \quad (15)$$

where

V_a^i = variance for path i

N = number of points in the satellite path i

η_j = linear friction coefficient for the procedure

η' = optimum value of η_j when V_a^i is minimized.

The optimum frictional coefficient η in equation (15) is assumed to be the true value that gives rise to the satellite recordings. In order to use equation (15), an initial equilibrium sea surface above the reference ellipsoid has to be adopted in order to bring the SEASAT–ALT observations to model datum. For this purpose, we used the mean sea surface SS3 constructed by Marsh & Martin (1982), using SEASAT ephemeris calculated by the Preliminary Gravity

Solution — SEASAT 3 (PGS—S3) and the SEASAT—ALT data from the interval July 28 — August 14. In their analysis Marsh & Martin (1982) combined the two data sets as accurately as possible, choosing a grid system which would yield global contour maps of the mean sea surface topography. Due to the possibility of icebergs, the data for the SS3 surface north of 68°N were set to zero.

Figs 15a—d display the variations of the variance V_a^i as a function of linear bottom stress coefficient for four SEASAT orbit tracks. The data used in the optimization procedure correspond to water depth greater than 90m (approximately 50 fathoms) to avoid any possible shallow water non-linear effects which could drastically change the results. The most common optimum value for the coefficient obtained from these paths (except path 9, revolution no. 765) is 0.255 cm s^{-1} . The result from path 9 shows an extraordinarily large value for the linear stress coefficient. This is attributed to the featurelessness of the residual sea surface after the removal of the SS3 surface from the SEASAT—ALT measurements. The residual sea surface has an almost constant sea-surface elevation and a large value of the stress coefficient is needed to generate such a surface numerically. Featurelessness of the residual sea surface occasionally occurs because the SS3 surface also contains a limited amount of information about the transient sea-surface variation, although it could possibly represent a long-term equilibrium surface. In this case, a different approach or other suitable representation method of the equilibrium sea surface is desired. Another aspect concerning the measurement of fitness is that the variance calculated using equation (15) is very sensitive to

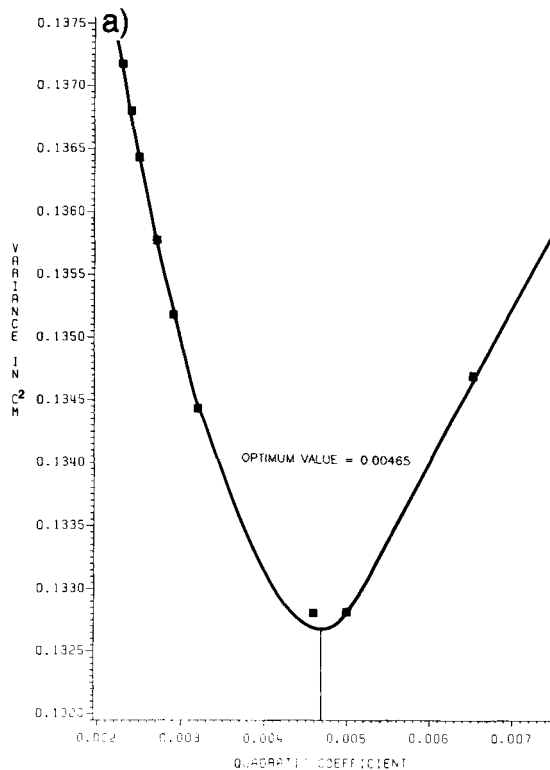


Figure 16. (and overleaf) Variance between simulated and observed transient sea-surface profiles as a function of the constant quadratic coefficient. Diagrams (a), (b), (c) and (d) correspond to revolutions nos 559, 564, 765 and 789.

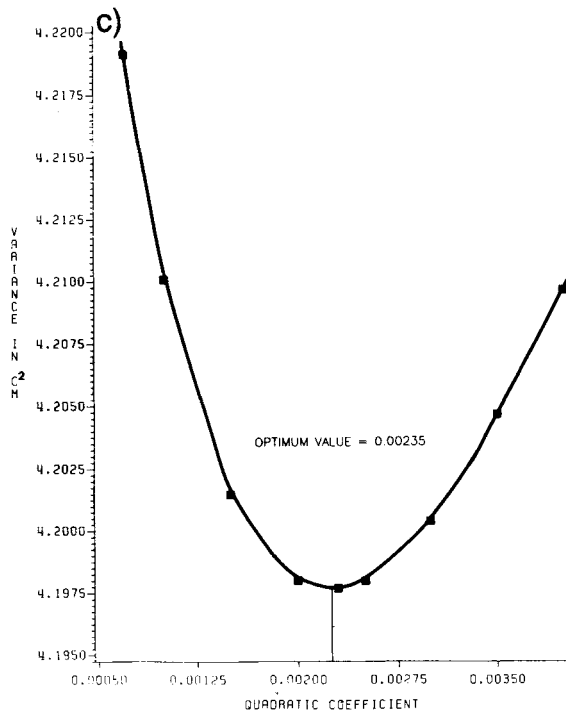
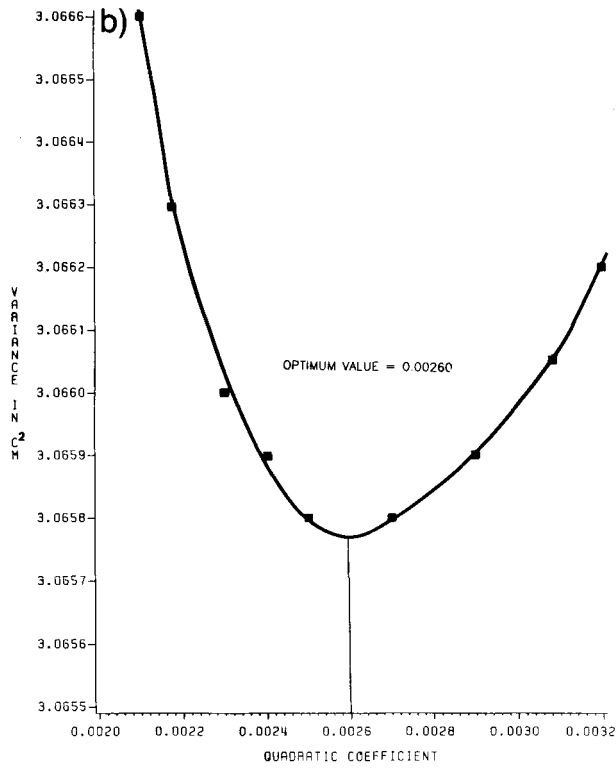


Figure 16 – continued

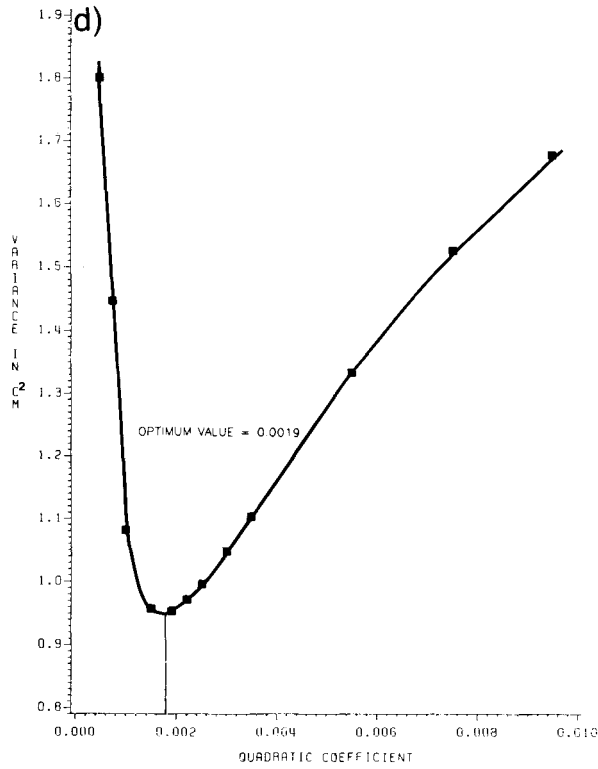


Figure 16 -- continued

uncertainties in observations and to numerical noise, even when the observations are in fairly good agreement with the model.

8.2 QUADRATIC BOTTOM FRICTION COEFFICIENT

The most commonly used ocean bottom frictional law expresses the bottom stress in terms of the square of the mean current velocity:

$$F_B = \frac{C\rho}{H^2} \bar{u} |\bar{u}|, \quad G_B = \frac{C\rho}{H^2} \bar{v} |\bar{v}|, \quad (16)$$

where C is the dimensionless quadratic stress coefficient, which traditionally takes values close to 0.0025. The handling of the quadratic frictional dissipation requires special attention to the water depth field. In shallow waters with water depth less than 2–4 m, there may be a problem with the stability of the equation of motion, and the resulting values of sea surface elevation and current could be unrealistically large. It should also be noted that the components \bar{u} and \bar{v} used in equation (16) are in the vicinity of the ocean bottom and cannot be arbitrarily replaced by the depth averaged current values without some assumptions. Kagan (1971) has summarized the published quadratic bottom stress coefficients since 1918, which range from 6×10^{-4} to 2×10^{-2} . It is also apparent that the quadratic bottom stress coefficient depends very much on the topography and on sediments deposited at the bottom of the ocean (Grant & Madsen 1979; Soulsby & Dyer 1981; Kemp & Simon 1984).

The procedure for estimating the quadratic bottom friction coefficient follows the same

steps as used for the linear friction coefficient. The ocean bottom frictional dissipative terms in the equations of motion are substituted by equation (16) and the modelling procedure is repeated with different quadratic coefficients C . The variance given by equation (15) as a function of C is depicted in Figs 16(a)–(d) for the SEASAT orbit tracks included in this study. The correlation result for path 9 (revolution no. 765) shows higher frictional dissipation as was found also in the case of linear friction. Such high dissipation value is due to the discrepancy between the SEASAT–ALT measurements and SS3 values along the orbit tracks. The mean value of the quadratic friction coefficient determined, including the unusually high results from path 9, is 0.00234, a value which is slightly smaller in magnitude than the traditionally adopted value of 0.0025.

9 Discussion

Dissipation of the ocean tide and pole tide (Wunsch 1974) depends greatly on the rate of bottom friction in shallow seas (Jeffreys 1921). The ocean bottom friction coefficient also plays an important role in oceanographic modelling studies such as tidal interaction and storm surge (Kinsman 1965; Pedlosky 1979). Since the pole tide can significantly modify the period of the Earth's wobble, and may also provide a damping mechanism, such an oceanographic–geophysical process will add to the importance of understanding of the ocean bottom coupling in a global perspective. The coupling mechanisms at the air–sea interface and at the ocean bottom are not yet fully understood, particularly in satellite applications. An understanding of the effects on the length of day of meteorological momentum transfer across the oceanic boundary layer required a detailed knowledge of frictional coupling mechanism at the air–sea interface and ocean bottom (Moon 1987).

Recently a considerable amount of work has been done on the effects of wind on the sea surface, and numerous empirical air–sea interface friction laws have been proposed (Brocks & Krugermeyer 1972; Garratt 1977; Smith 1980; Wu 1969, 1980, 1982; Ezraty 1985). The results of this research indicate that the wind speed coefficient formula proposed by Wu (1980, 1982) is consistently acceptable for the wind speed field selected. The geostrophically derived wind information from the MSL pressure charts adequately represent the surface wind field and is in a much more convenient form for input to the hydrodynamic modelling algorithm. The SEASAT–GDR wind speed data appear to be very erratic in several cases and were not used in this research.

The indirect method of estimating the ocean bottom friction coefficient was introduced in oceanography by Grace (1930) in his study of the Gulf of Suez. However, the scarcity of acceptable tidal or storm surge data prevented the wide acceptance of the method. The direct method of using measured current velocity data at particular regions has provided some valuable information, but as already indicated its main disadvantage has been the difficulty of installing a large number of ocean bottom current measuring devices around the world. Recent introduction of geophysical and oceanographic satellites has made it possible to estimate the ocean bottom friction coefficients using the indirect approach. Such determinations should certainly provide a global representation of the actual bottom frictional coupling mechanism if the data base is large enough (Moon *et al.* 1987). In this paper we have described how to obtain estimates of the ocean bottom friction coefficients by modelling an atmosphere–ocean coupled system (Hudson Bay area, Canada) and correlating and optimizing the results with the SEASAT–ALT data. The optimum linear and quadratic friction coefficients values obtained are 0.255 cm s^{-1} and 0.00234 respectively. Since these values were not directly affected by the ocean bottom topography and the physical and/or chemical constituents of the ocean bottom sediments (Grant & Madsen 1979; Kemp & Simon

1984), they represent global, rather than installation- and topography-dependent local values. In this respect, the ocean bottom friction coefficients determined by the indirect method employing satellite observations are the more meaningful values to use in global geophysical studies.

Acknowledgments

This research was supported by NSERC of Canada operating grant A-7400. The authors benefited greatly from discussions with Professors M. G. Rochester and Petr Vanicek. We thank Dr J. G. Marsh of the Goddard Space Flight Center (NASA) and Dr Nelson Freeman of RADARSAT Project Office (CCRS) for their many helpful suggestions. We are also indebted to Mr Barry Atkinson of the Atmospheric Environment Services (Canada), who kindly made the weather charts available.

References

- Andrews, J. T., 1974. *Glacial Isostasy*, Dowden, Hutchinson and Ross Inc., Pennsylvania.
- Bowden, K. F. & Fairbairn, L. A., 1956. Measurements of turbulent fluctuations and Reynolds stresses in a tidal current, *Proc. R. Soc. A*, **237**, 442–438.
- Brocks, K. & Krugermeyer, L., 1972. The hydrodynamic roughness of the sea surface, in *Studies in Physical Oceanography*, **1**, 75–92, ed. A. L. Gordon, Gordon and Breach Publishers, New York.
- Brosche, P. & Sunderman, J., 1978. *Tidal Friction and the Earth's Rotation*, Springer-Verlag, Berlin.
- Brown, G. S., Stanley, H. R. & Roy, N. A., 1981. The wind speed measurement capability of spaceborne radar altimeter, *IEEE J. Ocean. Eng.*, **OE-6**, 59–81.
- Cartwright, D. E. & Alcock, C. A., 1981. On the precision of sea surface elevations and slopes from SEASAT altimetry of the northeastern Atlantic ocean, in *Oceanography from Space*, pp. 885–895, ed. Gower, J. F. R., Plenum, New York.
- Cathles, L. M., 1975. *The Viscosity of the Earth's Mantle*, Princeton University Press, New Jersey.
- Ezraty, R., 1985. Etude de l'algorithme d'estimation de la vitesse de frottement à la surface de la mer, *Technical Report No. 6155/85/NL/BI*, IFREMER, 1–54.
- Fedor, L. S. & Brown, G. S., 1982. Wavelength and wind speed measurements from the SEASAT radar altimeter, *J. geophys. Res.*, **87**, 3254–3260.
- Freeman, N. G. & Murty, T. S., 1976. Numerical modelling of tides in Hudson Bay, *J. Fish. Res. Board Can.*, **33**, 2345–2361.
- Garratt, J. R., 1977. Review of drag coefficient over oceans and continents, *Mon. Weath. Rev.*, **105**, 915–929.
- Grace, S. F., 1930. The influence of friction on the tidal motion of the Gulf of Suez, *Mon. Not. R. Astr. Soc., Geophys. Suppl.*, **2**, 306–318.
- Grant, W. D. & Madsen, O. S., 1979. Combined wave and current interaction with a rough bottom, *J. geophys. Res.*, **84**, 1797–1808.
- Griffith, D. K., Pingree, R. D. & Sinclair, M., 1981. Summer tidal fronts in the near-Arctic regions of Fox Basin and Hudson Bay, *Deep Sea Res.*, **28a**, 865–873.
- Hasse, L. & Wagner, V., 1971. On the relationship between geostrophic and surface wind on sea, *Mon. Weath. Rev.*, **99**, 225–260.
- Heaps, N. S., 1965. Storm surge on continental shelf, *Phil. Trans. R. Soc. A*, **257**, 351–383.
- Heaps, N. S., 1969. A two-dimensional numerical sea model, *Phil. Trans. R. Soc. A*, **265**, 93–137.
- Heaps, N. S., 1982. Storm surges 1967–1982, *Geophys. J. R. astr. Soc.*, **74**, 331–376.
- Jeffreys, H., 1921. Tidal friction of shallow seas, *Phil. Trans. R. Soc. A*, **221**, 239–264.
- Kagan, B. A., 1971. Sea bed friction in one-dimensional tidal currents, *Izvestia, Atmospheric and Oceanic Physics*, **8**, 780–785.
- Kemp, P. H. & Simon, R. R., 1984. Sediment transport due to waves and tidal currents, in *Seabed Mechanics*, pp. 197–206, ed. Pennes, Bruce, Graham & Trotam, London.

- Kinsman, B., 1965. *Wind Waves: Their Generation and Propagation on the Ocean Surface*, Prentice-Hall Inc., Englewood Cliffs, NJ.
- Ku, L. F., 1982. Observed tide data in the Hudson Bay area of Canada (private communication).
- Ku, L. F., 1984. *Analysis of satellite altimeter data at crossing points* (internal report – draft), Canadian Hydrographic Service, Ottawa.
- Lambeck, K., 1975. Effects of tidal dissipation in the oceans on the Moon's orbit and the Earth's rotation, *J. geophys. Res.*, **80**, 2917–2925.
- Large, W. G., 1979. The turbulent fluxes of momentum and sensible heat over the open sea during moderate to strong wind, *PhD thesis*, University of British Columbia, Vancouver, Canada.
- Lorell, J., Parke, M. E. & Scott, J. F., 1980. SEASAT geophysical data record (GDR) user's handbook, *JPL Intern. Report 622–97*, Pasadena, Calif.
- Marsh, J. G. & Martin, T. V., 1982. The SEASAT altimeter mean sea surface model, *J. geophys. Res.*, **87**, 3269–3280.
- Marsh, J. G. & Williamson, R. G., 1980. Precision orbit analyses in support of the SEASAT altimeter experiment, *J. astronaut. Sci.*, **28**, 345–369.
- Moon, W., 1984. Transient sea surface height variation and the SEASAT–ALT data application, *Proc. 8th Canadian Symp. on Remote Sensing*, pp. 273–282.
- Moon, W. & Tang, R., 1984a. Ocean bottom friction study from numerical modelling of the SSH and SEASAT–ALT data, *J. Mar. Geophys. Res.*, **7**, 73–76.
- Moon, W. & Tang, R., 1984b. On the hydrodynamic correction of SEASAT–ALT data and geodynamic applications, *European Space Agency SP-215*, 553–557.
- Moon, W. & Tang, R., 1985. On the hydrodynamic correction of SEASAT–ALT data (Hudson Bay area of Canada), *M. Geodesy*, **9**, 291–333.
- Moon, W., Tang, R. & Choi, B. H., 1986. Study of ocean bottom coupling coefficient in East China Sea (in preparation).
- Moon, W., 1987. On the coupling processes at geophysical boundaries (in preparation).
- Munk, W. H. & MacDonald, G. J. F., 1960. *The Rotation of the Earth: A Geophysical Discussion*, Cambridge University Press.
- Pedlosky, J., 1979. *Geophysical Fluid Dynamics*, Springer-Verlag, New York.
- Pekeris, C. L. & Accad, Y., 1969. Solution of Laplace's equation for the M2 tide in the world oceans, *Phil. Trans. R. Soc. A*, **265**, 413–436.
- Ramming, H. G. & Kowalik, Z., 1980. *Numerical Modelling of Marine Hydrodynamics*, Elsevier, New York.
- Schwiderski, E. W., 1978. Global ocean tides, Part 1. A detailed hydrodynamic interpolation model, *NSWC/DL, Tr-3866*, Naval Surface Weapons Center, Dahlgren, Virginia.
- Simmons, T. J., 1980. Circulation models of lakes and inland seas, *Can. Bull. Fish. Aquat. Sci.*, **203**, Ottawa, Canada.
- Smith, S. D., 1980. Wind stress and heat flux over the ocean in gale force winds, *J. phys. Oceanogr.*, **10**, 709–726.
- Soulsby, R. L. & Dyer, K. R., 1981. The form of the near-bed velocity profile in tidally accelerating flow, *J. geophys. Res.*, **86**, 8067–8074.
- Sternberg, R. W., 1968. Friction factors in tidal channels with differing bed roughness, *Mar. Geol.*, **6**, 243–260.
- Stock, G. G., 1976. Modelling of tides and tidal dissipation in the Gulf of California, *PhD Dissertation*, University of California, San Diego.
- Tapley, B. D., Born, G. H. & Parke, M. E., 1982. The SEASAT altimeter data and its accuracy assessment, *J. geophys. Res.*, **87**, 3179–3188.
- Thompson, R. E., 1983. A comparison between computed and measured oceanic winds near the British Columbia coast, *J. geophys. Res.*, **88**, 2675–2683.
- Weenink, M. P. H., 1958. *A theory and method of calculation of wind effects on sea levels in a partly enclosed sea, with special application to the southern coast of the North Sea*, Koninklijk Nederlands Meteorologisch Instituut, Mededelingen en Verhandelingen, No. 73.
- Wentz, F. J., Cardone, V. J. & Fedor, L. S., 1982. Intercomparisons of wind speeds inferred by the SASS, Altimeter and SMMR, *J. geophys. Res.*, **87**, 3378–3384.
- Wu, J., 1969. Wind-stress and surface roughness at air–sea interface, *J. geophys. Res.*, **74**, 444–455.
- Wu, J., 1980. Wind-stress coefficients over sea surface near neutral conditions: A revisit, *J. Phys. Oceanogr.*, **10**, 727–747.
- Wu, J., 1982. Wind-stress coefficients over sea surface from breeze to hurricane, *J. geophys. Res.*, **87**, 9704–9706.

- Wunsch, C., 1974. Dynamics of Pole tide and the damping of the Chandler wobble, *Geophys. J. R. astr. Soc.*, **39**, 413–419.
- Zahel, W., 1978. The influence of solid Earth deformations on semidiurnal and diurnal oceanic tides, in *Tidal Friction and Earth's Rotation*, pp. 98–124, eds Brosche, P. & Sundermann, J., Springer-Verlag, New York.